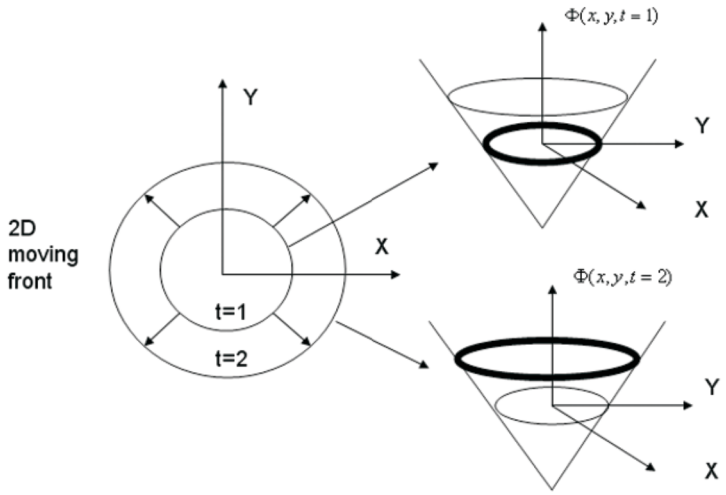

Figure 1. The level set function.

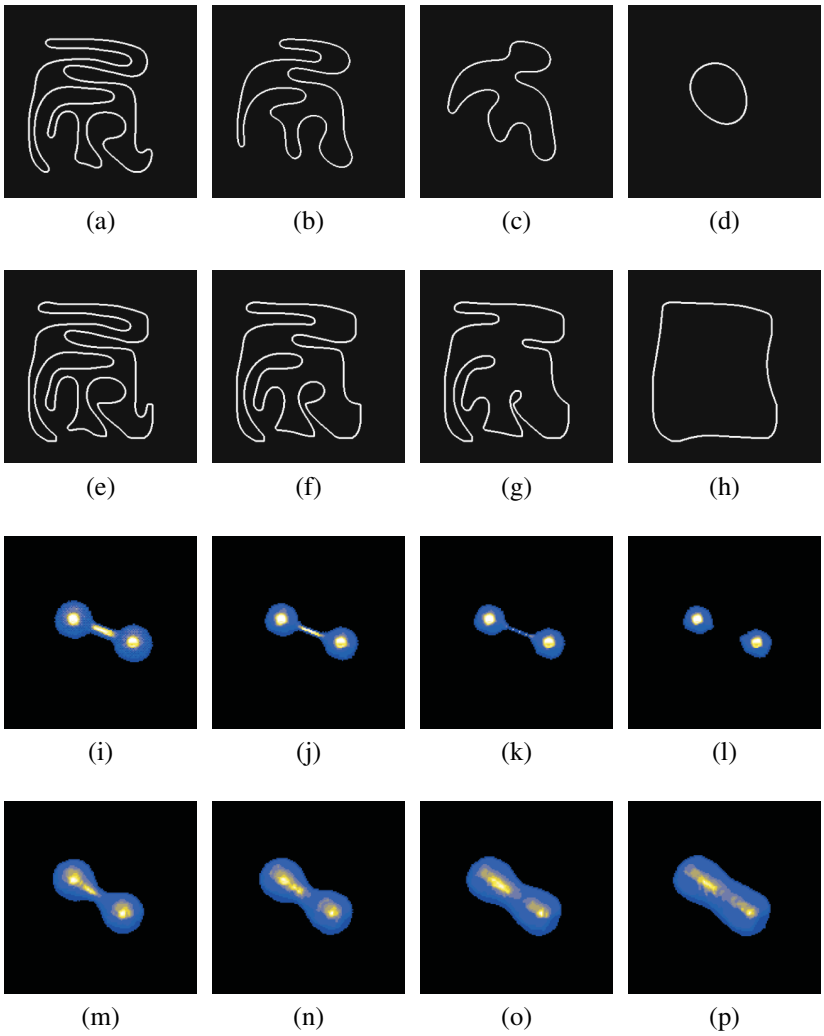

Figure 2. Propagation of the closed 2D curve and 3D surface: (a) under curvature at iteration 100; (b) under curvature at iteration 2000; (c) under curvature at iteration 4000; (d) under curvature at iteration 17000; (e) under negative curvature at iteration 100; (f) under negative curvature at iteration 2000; (g) under negative curvature at iteration 4000; (h) under negative curvature at iteration 17000; (i) under curvature at iteration 100; (j) under curvature at iteration 2000; (k) under curvature at iteration 4000; (l) under curvature at iteration 17000; (m) under negative curvature at iteration 100; (n) under negative curvature at iteration 2000; (o) under negative curvature at iteration 4000; (p) under negative curvature at iteration 17000.

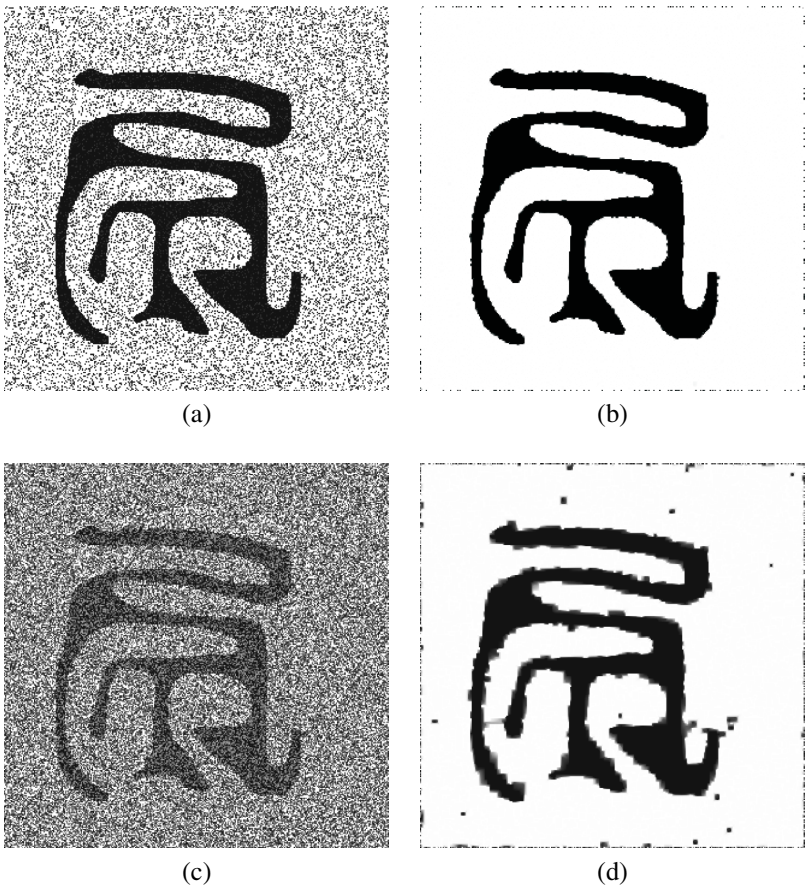

Figure 3. Noise removal and segmentation via moving under curvature: (a) image with mild noise; (b) after removing the noise; (c) image with strong noise; (d) after removing the noise.

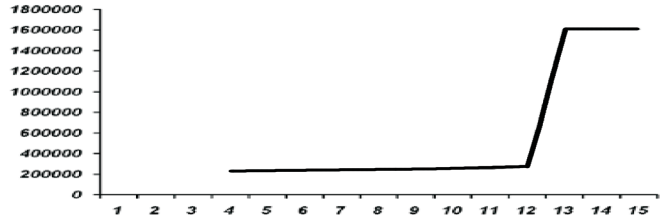

Figure 4. Number of voxels visited by the front using different threshold values.

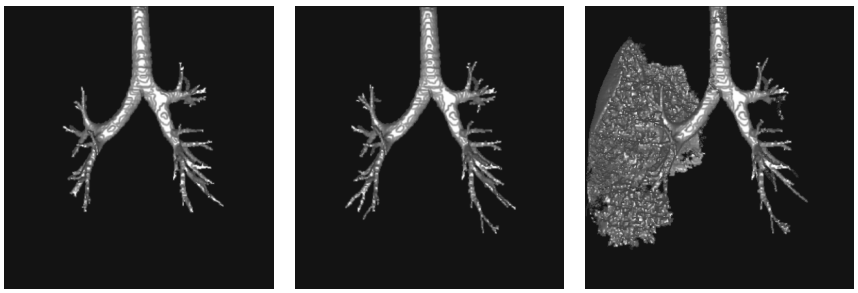

(a) (b) (c)

Figure 5. Pulmonary airway tree segmentation using 3D Fast Marching Methods: (a) result using stopping criterion as 6 in gray value; (b) result using stopping criterion as 11 in gray value; (c) result using stopping criterion as 13 in gray value.

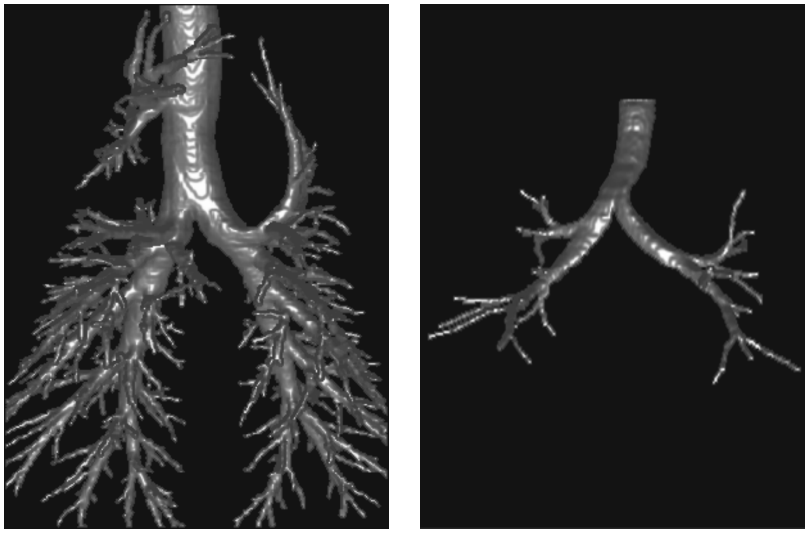

(a) (b)

Figure 6. Results of pulmonary airway tree segmentation using 3D Fast Marching Methods from 3D CT image data: (a) pulmonary airway tree of a sheep lung from 3D CT data; (b) pulmonary airway tree of a human lung from low-dose 3D CT data.

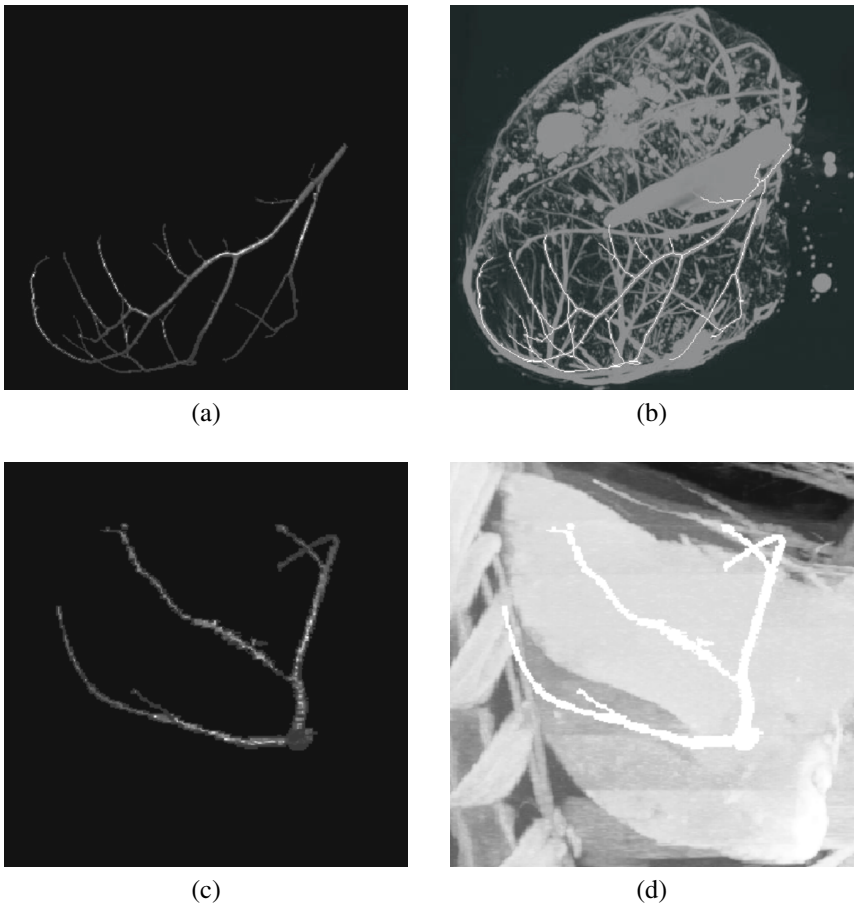

Figure 7. Comparison between 3D Fast Marching Methods for coronary artery segmentation and Maximum Intensity Projection: (a) segmentation result for the coronary artery tree of a mouse heart from 3D micro CT data; (b) Maximum Intensity Projection of the original data with skeleton; (c) segmentation result for the coronary artery tree of a sheep heart from 3D CT data; (d) Maximum Intensity Projection of the original data with segmentation.

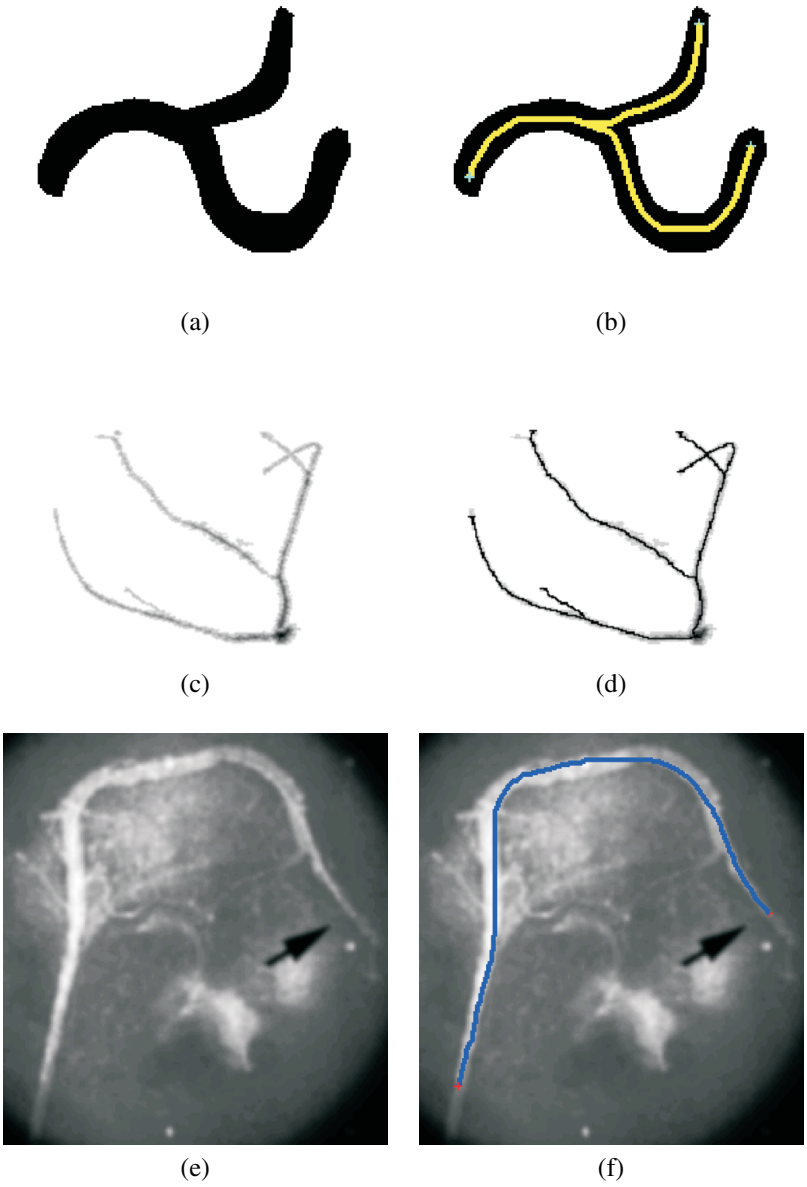

Figure 8. Centerline extraction and optimal path finding; (a) original 2D binary image; (b) centerline extracted using distance information; (c) inverse of 3D distance map corresponding to the segmented coronary artery from sheep heart in Figure 7c; (d) 3D centerline extracted from the inverted distance map; (e) original angiographic image; (f) path found by using gray value as cost.

(a) (b)

Figure 9. Image inpainting using level set methods: (a) corrupted image; (b) restored image after the fast marching-based inpainting.

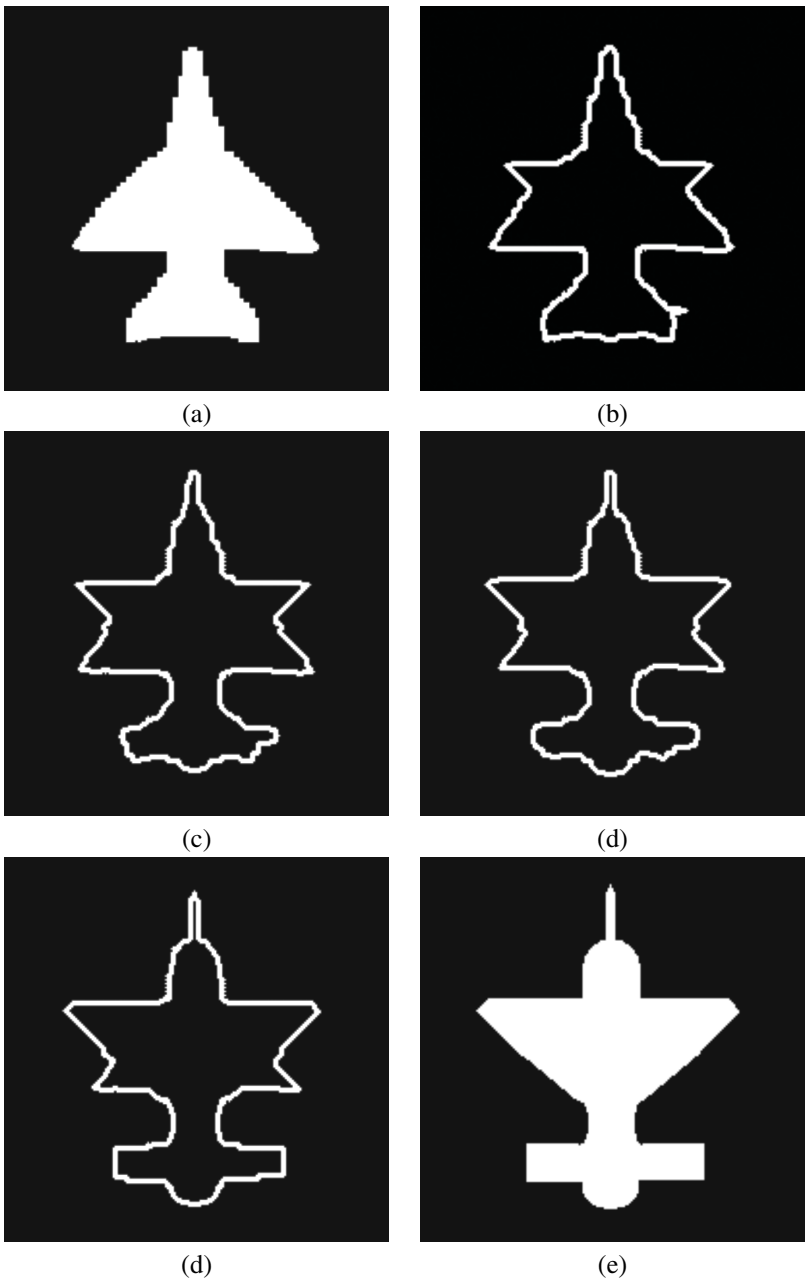

Figure 10. Metamorphosis using level set methods: (a) original shape; (b) interim step 1; (c) interim step 2; (d) interim step 3; (e) interim step 4; (f) final target shape.

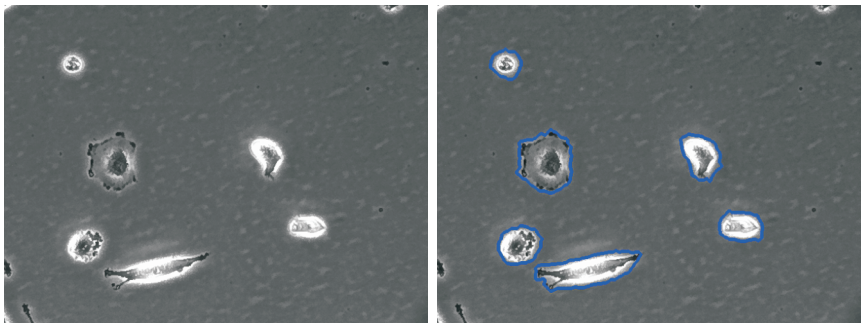

(a) (b)

Figure 11. Using the front-evolving geometric model for segmentation of living tumor cells in the LSDCAS system: (a) original image; (b) result.

(a) (b) (c) (d) (e)

Figure 12. Weak boundary enhancement: (a) original image with partial weak edge; (b) gradient of original image; (c) new image after enhancement; (d) segmentation result using a front-evolving model on original image; (e) segmentation result using a front-evolving model on the enhanced image.

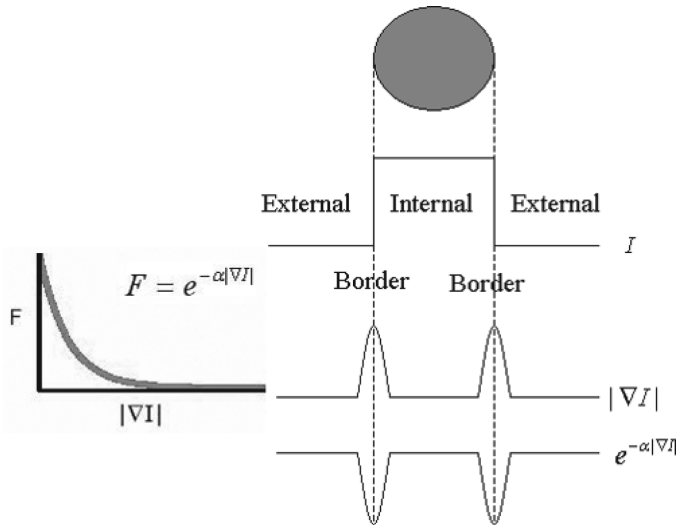

Figure 13. Typical definition of the edge functions to control propagation of the moving front.

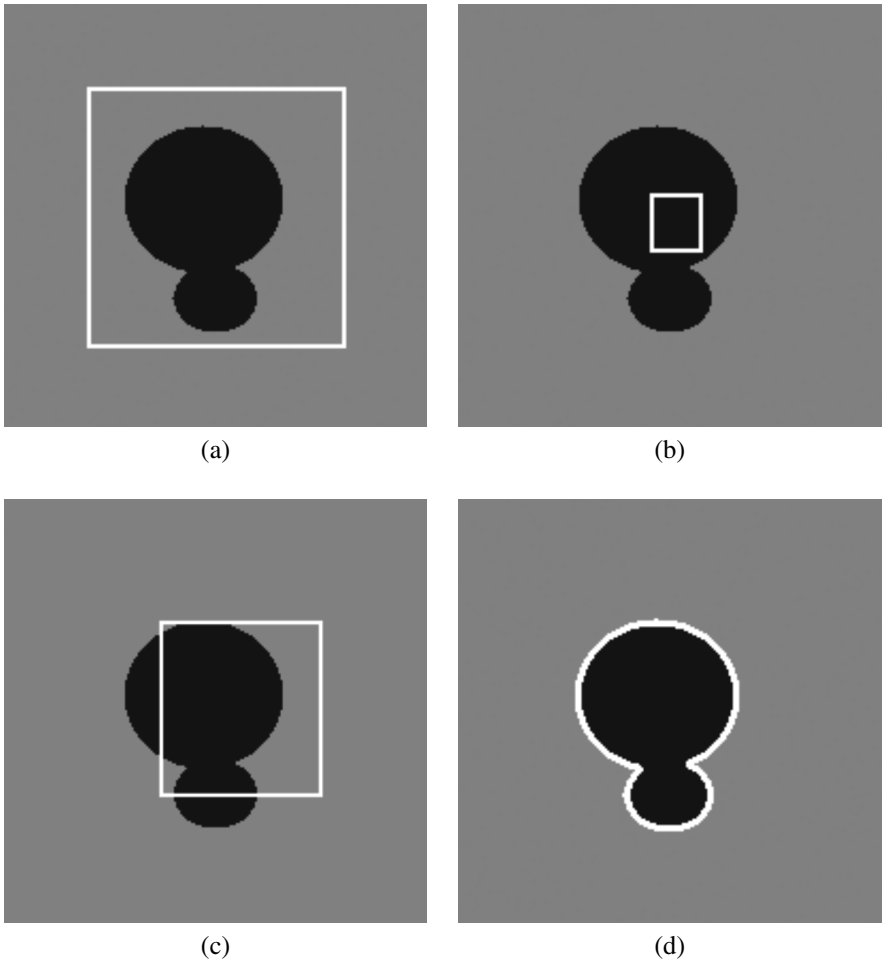

Figure 14. Consider all possible cases in the position of the curve. The fitting term is minimized only in the case when the curve is on the boundary of the object. (a) The curve C is outside the object, and $F_1(C) > 0$ and $F_2(C) \approx 0$. (b) The curve C is inside the object; then $F_1(C) \approx 0$ and $F_2(C) > 0$. (c) The curve C is both inside and outside the object; then $F_1(C) > 0$ and $F_2(C) > 0$. (d) The fitting term is minimized when the curve C is on the boundary of the object.

(a) (b) (c)

Figure 15. Segmentation using a region-based active contour: (a) original image; (b) image with initial contour; (c) image with segmentation result.

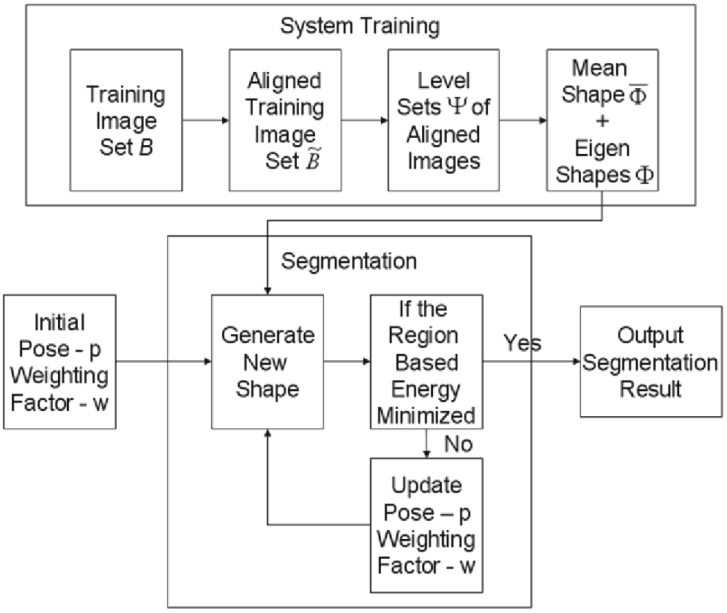

Figure 16. Flowchart of the algorithm presented in [**?**]. Basically, there are two stages. The first stage is system training to extract shape model, and the second is to segment the image using the shape model.

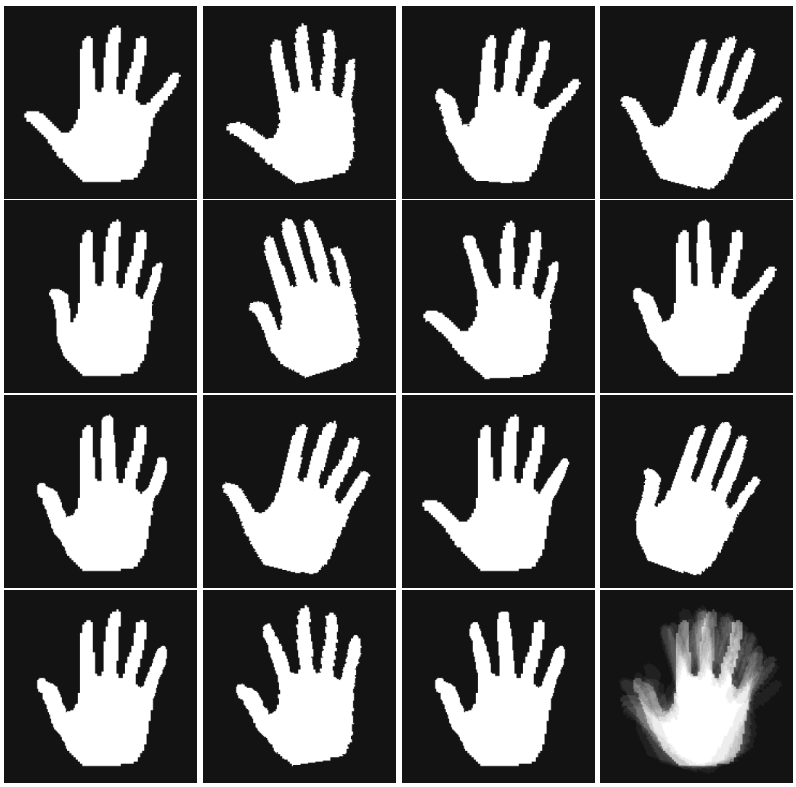

Figure 17. Binary images for training before alignment. The last image is the overlapping image before alignment.

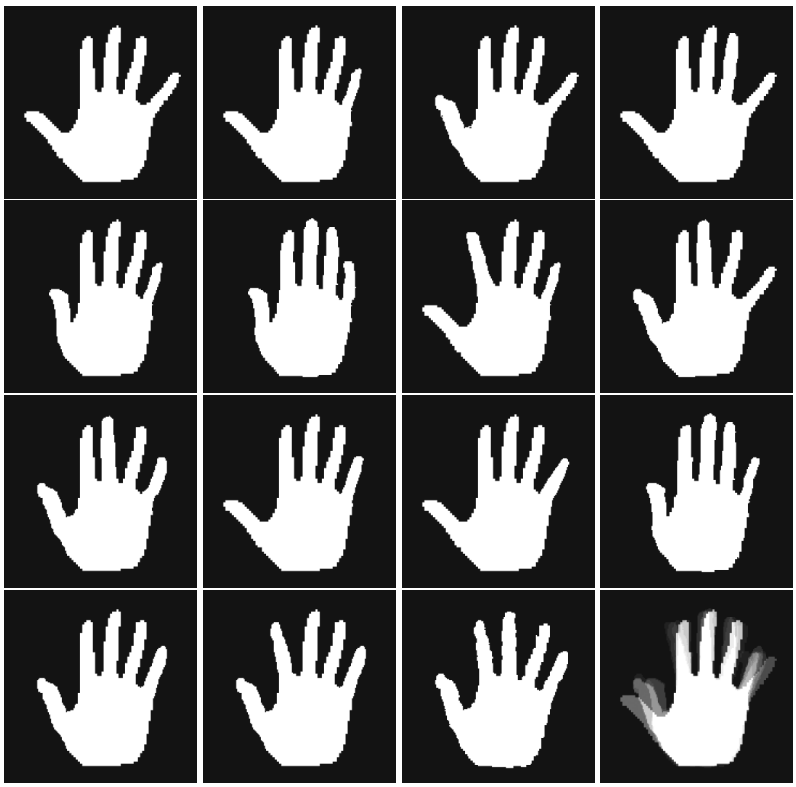

Figure 18. Binary image after alignment. The last image is the overlapping image after alignment.

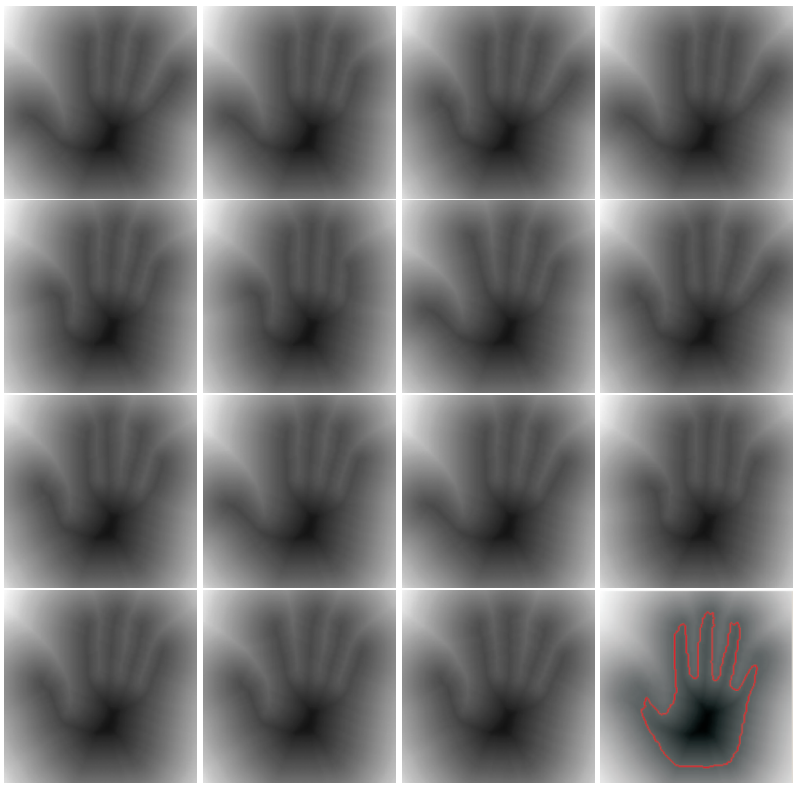

Figure 19. The level set for each image after alignment. The last image is the average level set, overlapped with the average shape after training.

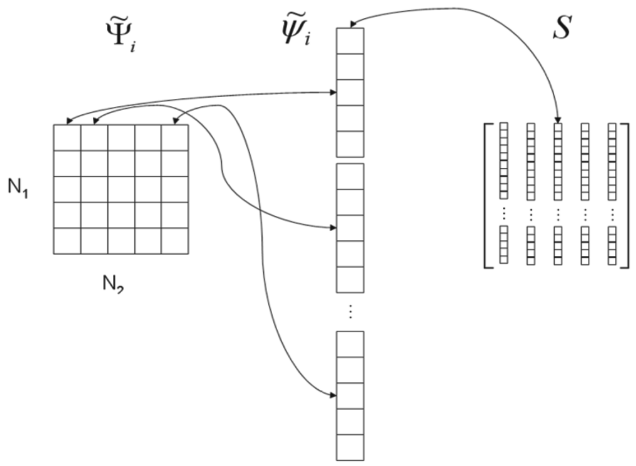

Figure 20. Creating the shape-variability matrix S.

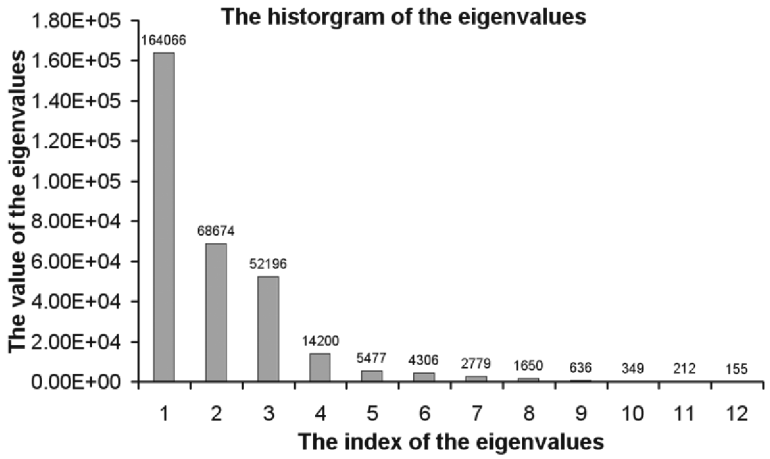

Figure 21. Histogram of the first 12 eigenvalues after PCA analysis on the 12 hand images.

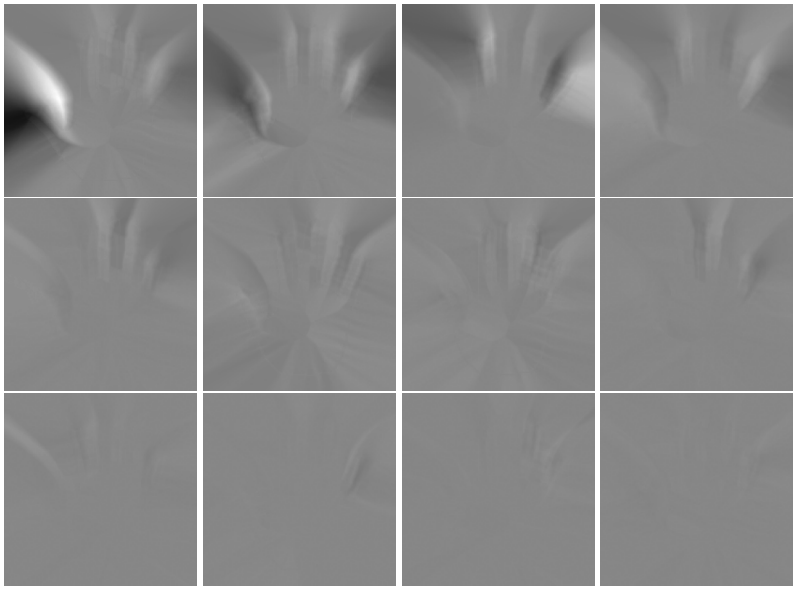

Figure 22. Output eigenshapes that have been scaled into the 0–255 range for illustration. Correspondingly, the largest 12 eigenvalues are 164066, 68674, 52196, 14200, 5477, 4306, 2779, 1650, 636, 349, 212, and 155. The smaller the value of the eignvalues, the smaller roles the eigenshapes will play in shape variation.

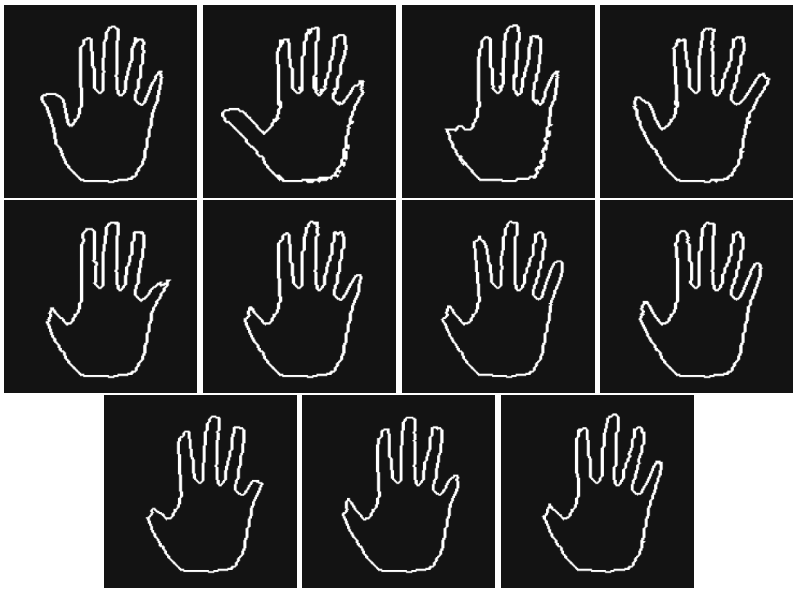

Figure 23. The first row is the shape after using the weight factor only from the first eigenshape. From left to right, the values of w are -0.3 and 0.3. The second row is the shape after using the weight factor only from the second eigenshape, and the same for other rows. The only image in the second column is the average shape without any shape variations.

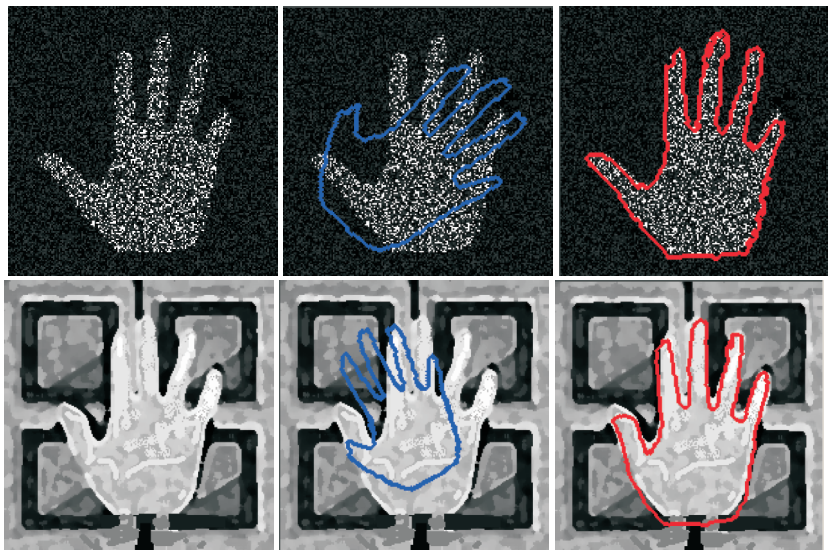

Figure 24. Segmentation using shape prior active contour. The first column includes the original noisy images for segmentation. The second column shows the images overlapped with initial average shape. The third column are the images with the final segmentation results.

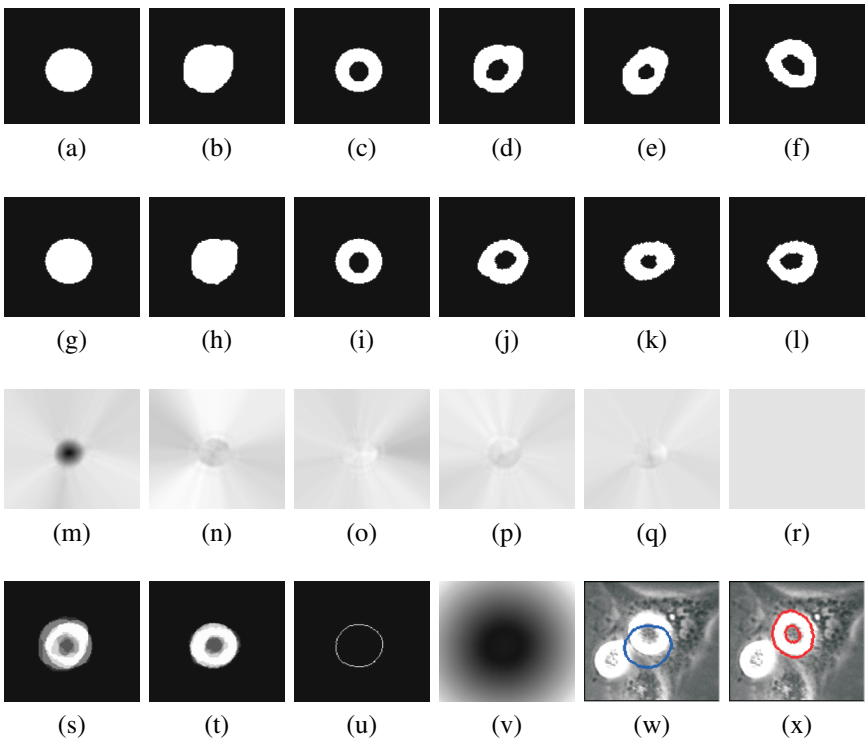

Figure 25. Segmentation using shape prior active contour: (a–f) images for training; (g–l) aligned training images; (m–r) eigenvectors after principal components analysis; (s) overlap before aligning; (t) overlap after aligning; (u) zero level set of the mean shape; (v) level set of mean shape; (w) target image to be segmented with initial contour; (x) segmentation result.

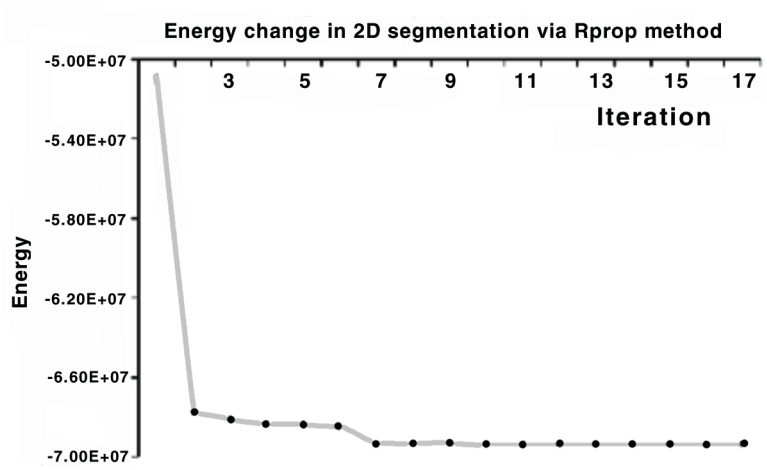

Figure 26. The region-based energy is decreasing as the Rprop method is applied for the 2D model-based segmentation.

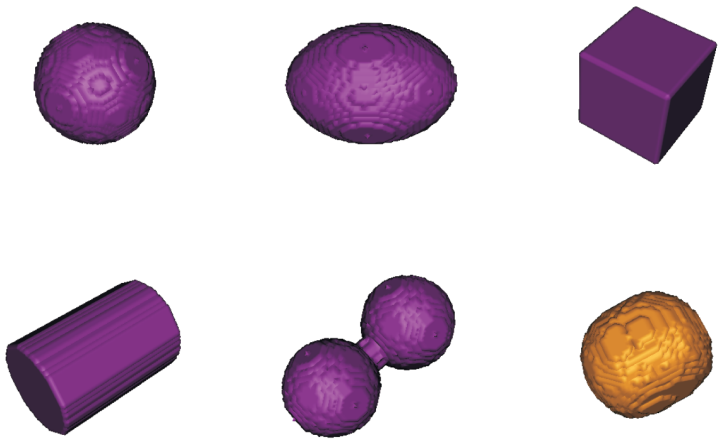

Figure 27. 3D images for training before alignment. The last image is the average 3D shape after training.

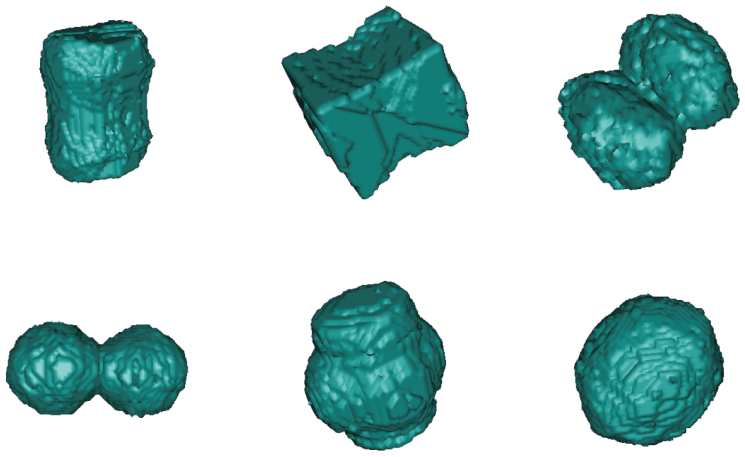

Figure 28. The first column are the two new shapes using the weight factor only from the first eigenshape, $+1$ and -1; correspondingly, the second column are the new shapes using the weight factor only from the second eigenshape, and the third column are from the third.

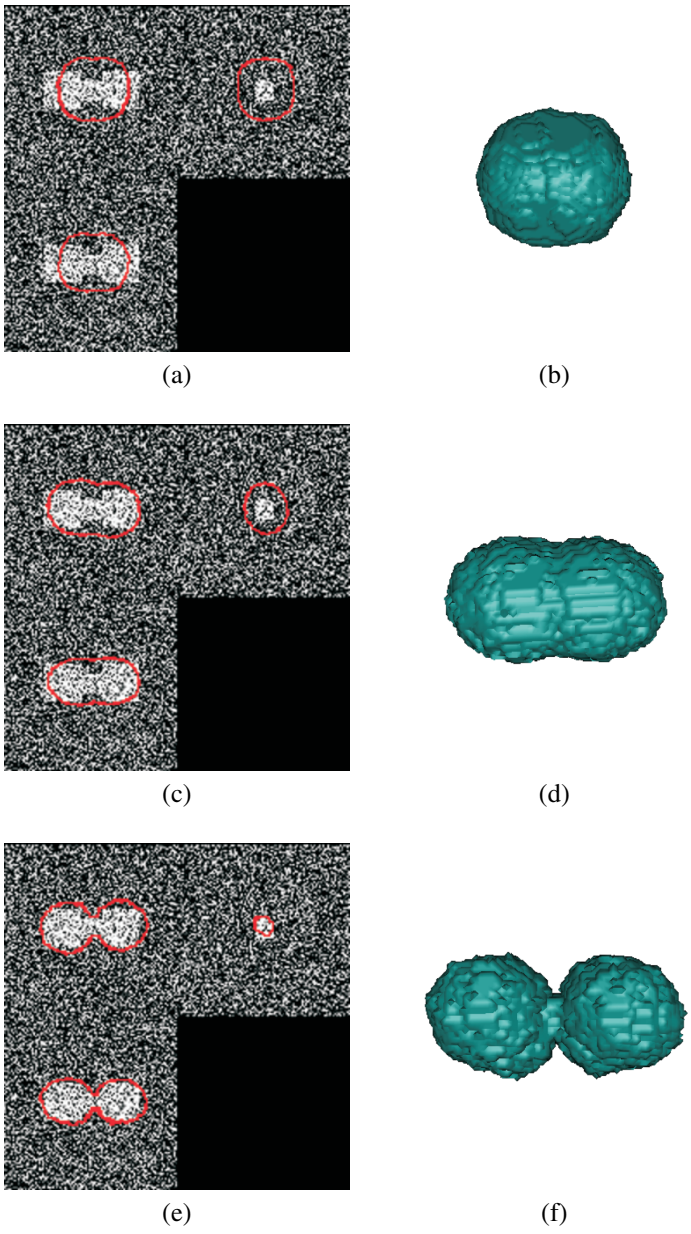

Figure 29. Example of 3D shape model-based segmentation: (a) three views of the original image to be segmented and the initial 3D average shape overlaid inside; (b) average 3D shape after surface rendering; (c) 3D surface at an interim step of the segmentation overlaid inside the original image; (d) surface rendering of the current 3D shape; (e) three views of the final segmentation; (f) surface rendering of the final segmentation.

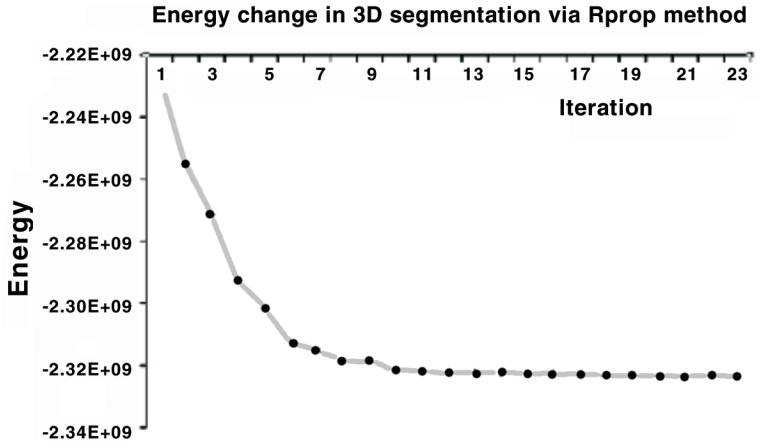

Figure 30. The region-based energy is decreasing as the Rprop method is applied for the 3D model-based segmentation.